Progress In Electromagnetics Research C, Vol. 108, 147–158, 2021

Fully Metallic Dual-Band 3-D Wire Antenna for Wi-Fi and Wi-MAX Applications

Fateh Benmahmoud[1, *], Pierre Lemaitre-Auger[2], and Smail Tedjini[2]

Abstract—A segmented three-dimensional wire monopole antenna is proposed and optimized to operate in both the Wi-Fi and Wi-Max frequency bands (2.4–2.48 and 3.3–3.7 GHz). The fabrication of the antenna employs both three dimension printing and foundry techniques. The design occupies a total volume of 33.8 mm × 30.4 mm × 37.4 mm, which is equivalent to $0.28\lambda_0 \times 0.25\lambda_0 \times 0.30\lambda_0$, where λ_0 is the central wavelength of the lower band. The measurements agree with the simulations and show that the antenna has a −10 dB impedance bandwidth of 7.53% (2.36 to 2.55 GHz) and 53.87% (2.78 to 4.43 GHz) and a measured −3 dB axial ratio bandwidth of 19.06% (3.18 to 3.85 GHz) for the second band. For the first band, simulations indicate that the polarization is elliptical. The radiation pattern is a near hemispherical coverage toward the upper hemisphere. The measured maximum gain values are 5.6 and 7.3 dB for the lower and upper bands, respectively. The simulated radiation efficiency is higher than 98%.

1. INTRODUCTION

Currently, both research and industrial communities pay a lot of attention to the internet of things (IoT). In the next generation of wireless networks, connected devices will constitute billions of intelligent autonomous communicating devices. So, it is important and interesting to develop hybrid architectures and solutions to operate within heterogeneous networks (HetNet) [1]. HetNet represents a key concept for the IoT, where many wireless technologies must coexist. It gives flexibility to the user to select the desired connectivity based on the application demands and the environmental conditions [2–6]. For some of those HetNet based on two communication protocols, the quality of the communication relies, among other things, on a dual-band antenna. Indeed, employing such an antenna reduces the occupied volume, cost, and complexity. This has been done for many protocols combinations such as Wi-Fi/Wi-Max [2–6], LoRa/Wi-Fi/BLE [7], LoRa/IEEE802.15.4 [8], and Zigbee/GPRS [9].

Given the fact that an IoT can be quite challenging, antennas as devices are usually exposed to electromagnetic phenomena such as depolarization and multi-path interferences during their normal operation. This harsh environment can have a significant impact on the reliability of the wireless system [10] if it is not taken into account. In such situations, having circularly polarized (CP) antennas makes the system more robust than using linearly polarized (LP) antennas. However, it is not an easy task for small dual-band antennas.

Diverse types of dual-band CP designs have been reported in the literature, usually characterized by a unidirectional radiation pattern. Multilayer stacked slot patch antennas of various shapes were designed for different applications like RFID UHF (824–849 MHz and 918–929 MHz) or Beidou navigation satellite system (1.61 and 2.49 GHz) [11–13]. The radiation efficiency of such antennas greatly depends on the used substrate. For the cited references, it is around 70%. A different approach was used; it consists of a combination of metasurface structures (MS) and slots or patch radiators

Received 16 November 2020, Accepted 5 January 2021, Scheduled 11 January 2021
* Corresponding author: Fateh Benmahmoud (benmahmoud.fateh@gmail.com).
[1] Ecole militaire Polytechnique, Algiers, Algeria. [2] Univ. Grenoble Alpes, Grenoble INP, LCIS, Valence 26000, France.

(2.5 and 3.5 GHz) [14] (1.88 and 2.5 GHz) [15]. The antennas were designed using low loss tangent substrates of 0.0021 and 0.0012, respectively. Other interesting single-layer dual-band antennas were also studied with various designs: eccentric rings (2.1 and 3.6 GHz with 80% efficiency) [16], substrate integrated waveguide (8.84 and 9.59 GHz, efficiency higher than 92%) [17], and magnetoelectric (ME) dipole antenna (2.93 and 5.35 GHz, efficiency higher than 95%) [18]. Electric and magnetic dipoles are combined in the literature. The ME dipole design is very efficient; however, its bulky profile ($0.98\lambda_0 \times 0.98\lambda_0 \times 0.30\lambda_0$) makes it only suitable for applications where size and volume are not a constraint. Finally, in [19], a crossed dipole structure is employed to achieve dual-band CP properties (2.5 and 3.5 GHz). The cited works above employ dielectrics substrates which reduce the radiation efficiency. They have narrow bandwidths impedance at -10 dB, and the highest values are 21.2% and 9.8% for the [19] case and a -3 dB axial ratio bandwidth (ARBW), $< 4.2\%$ in [15]. The MS dipole [18] is the exception with high efficiency and relatively large ARBW (29.1% and 13.1%), but it occupies a much higher volume.

We propose to use a three dimension (3-D) fully metallic segmented monopole antenna to obtain a small size dual-band antenna with CP. The targeted communication protocols are the Wi-Fi (2.4–2.48 GHz) and Wi-Max (3.3–3.7 GHz). Wi-Max is interesting for its long communication range and high data rate. A dual-band antenna for two protocols is interesting, for example, for drones or unmanned ground/surface vehicles to transmit video data in an interior or exterior environment.

Segmented monopole antenna was first proposed in [20]. It is made up of straight segments over a ground plane. Each segment is oriented arbitrarily in space. With the large degree of freedom during the antenna conception by dint of the third dimension, it is possible to achieve several different characteristics at the same time [21, 22]. This advantage is even more apparent when it comes to problems that present very conflicting requirements [23]. In addition, it has a high radiation efficiency because of the absence of dielectric material. This antenna structure was used in a variety of applications. In [24–28], the miniaturization concept was studied. It showed that this antenna topology could reach high compactness while maintaining good radiation properties. In [28], the measured -3 dB impedance bandwidth was 8.5% for an occupied volume as small as $(\lambda/12)^3$. In [29], an impedance-loaded wideband antenna was designed. It covered the frequency band 300 MHz to 15 GHz with a VSWR below 4.5. More achievements that target desired space coverage, CP, and high gain were accomplished in several works [30–36].

The 3-D wire antenna offers many features that qualify it as a solution to many applications. It exhibits a high radiation efficiency thanks to its dielectric-free structure. Its fully metallic structure allows it to operate in harsh environments (e.g., high temperatures). Its light weight makes it very suitable for aerospace applications where weight is a determinant factor. Compared to the previous works related to segmented wire antennas, the proposed antenna has addressed the problem of dual bands, which is a very challenging aspect to consider when dealing with restrain-size fully metallic wire-based antennas. We have also adopted a new foundry-based process coupled with 3-D printing fabrication technique to manufacture the desired shape. Compared with the previous works where wire folding techniques have been used, the employed technique has given us more accurate prototypes and the possibility to realize complex 3-D wire topologies.

The proposed antenna has a size $(< \lambda_0/3)^3$, where λ_0 is the wavelength at 2.45 GHz. It does not require a matching circuit. It is designed with a multi-objective genetic algorithm (MOGA) [37].

The antenna designed and its fabrication are presented in Section 2. In Section 3, the simulated and measured results are compared and analyzed. Concluding remarks are discussed in the last section.

2. ANTENNA DESIGN AND RESULTS

2.1. Design Technique

The multi-segment wire antenna is primarily a monopole antenna. Each segment is defined by an arbitrary orientation in space, angles ϕ and θ, and length d as shown in Figure 1. All the segments have the same radius, r. An antenna is considered geometrically correct if it respects the following conditions: no intersection between any non-consecutive segments, all the segments are above the ground plane ($z > 0$) and do not intercept it. The minimum angle between two consecutive segments is set to be higher than or equal to 20°. This limitation allows for easier fabrication by avoiding very fragile

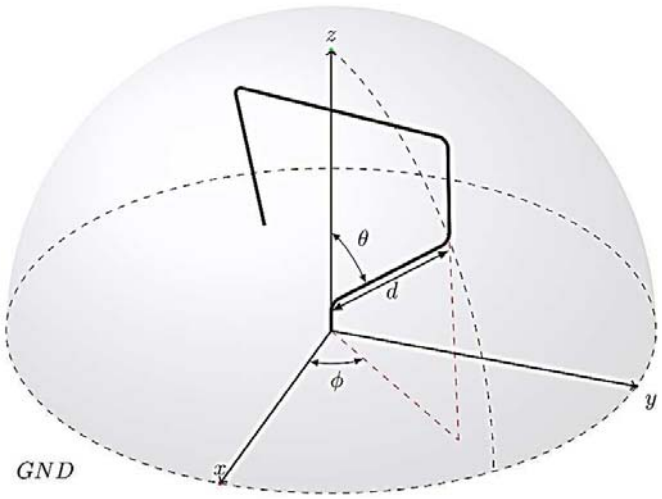

Figure 1. Parametrization of the 3-D antenna.

tapered angles. The maximum volume is fixed to $0.3\lambda_0 \times 0.3\lambda_0 \times 0.3\lambda_0$, where λ_0 is the wavelength at 2.45 GHz. The radius of each segment is fixed to $r = 0.7$ mm according to our fabrication capabilities. The shortest straight segment length is set to $4r$ (2.8 mm). These constraints are required to avoid complex and unrealizable structures, to target a reasonable volume occupied by the antenna and to decrease simulation time.

Each segment of an antenna structure was coded by three geometrical dimensions (three genes): its length, d_i, its elevation and azimuth angles, θ_i and ϕ_i, respectively. It was shown in [38] that it is more efficient for the GA to use real values than binary-coded values for the parameters. A vector of $3 \times N$ parameters defines the whole antenna where N is the number of segments. In the present case, it is fixed to 10. The real-valued chromosome considerably reduces the number of genes required to specify the design and makes the solution space easier to search. The implemented optimization tool is based on MOGA. Contrary to the simple genetic algorithm, MOGAs target to optimize more than one objective function without the need to regroup them all in a single weighted objective function [39]. This is adequate in the present case; each target frequency is an objective, and the axial-ratio over a bandwidth is another objective.

The MOGA starts by generating random M structures called individuals. After evaluating the objective functions, a selection phase is performed. This selection is based on the concepts of non-dominated sorting [40], where the population of individuals are classified into a hierarchy of sub-populations based on the ranking of Pareto efficiency. The closer an individual is to the Pareto-optimal front, the higher the probability is to participate in the creation of the next generation. A Pareto-optimal solution is defined as the best achievable value for one objective without deteriorating at least one of the other objectives [41]. The crowding distance criterion [42] is implemented in order to maintain the diversity in each generation and to avoid the convergence to very similar solutions. Table 1 shows the fitness functions used.

The first two objective functions aim to set the antenna matching to a 50 ohms source at the Wi-Fi and Wi-Max bands. In Table 1, Δf_{r1} and Δf_{r2} represent the two target frequency intervals, 2.4 to 2.48 GHz and 3.3 to 3.7 GHz, respectively. The axial ratio criterion was applied only on the Wi-Max

Table 1. Objective functions.

	Expression
f_1	$\overline{\lvert S_{11}\rvert}$ (@Δf_{r1})
f_2	$\overline{\lvert S_{11}\rvert}$ (@Δf_{r2})

frequency band. This compromise has to be done to obtain a higher miniaturization factor and a larger ARBW on the second band, where the communication rate is the highest. CP is thus more important for the second band than for the first one. A sample was considered every 10 MHz and 100 MHz to evaluate the fitness functions within the two frequency bands, Δf_{r1} and Δf_{r2}, respectively.

The optimization tool evaluates the electromagnetic performances of all the individuals of a generation. The simulation conditions were simplified to speed up the optimization process by the use of a perfect ground plane and the absence of a connector. Also, all metallic parts are considered to be perfect conductors (PECs). Then, the MOGA selects the individuals that are the closest to the Pareto front (i.e., the best solutions) according to the fitness functions while respecting the crowding distance criterion. Each of the 50% best-selected individual has a chance to be involved in the process of cross-over to create the next generation with a probability of 70%. It could also go through a mutation with a probability of 10%. The number of individuals per generation is fixed to 120.

After 637 generations, no significant enhancement could be detected anymore among the best individuals of the last ten generations. The optimization was stopped, and only one structure was chosen. The chosen structure is simulated again in more realistic conditions: with a finite ground plane of 150 mm × 150 mm and an SMA connector. Also, during the optimization process, it was discovered that the minimum radius that could be used was 0.9 mm and not 0.7 mm like it was initially planned. The increase of the antenna radius by 0.2 mm was necessary to solidify the antenna body during the fabrication process. This radius modification was taken into consideration in the final simulated model. This new radius value was used. Finally, the properties of annealed copper were used for the metal parts. Figure 2 shows the chosen structure.

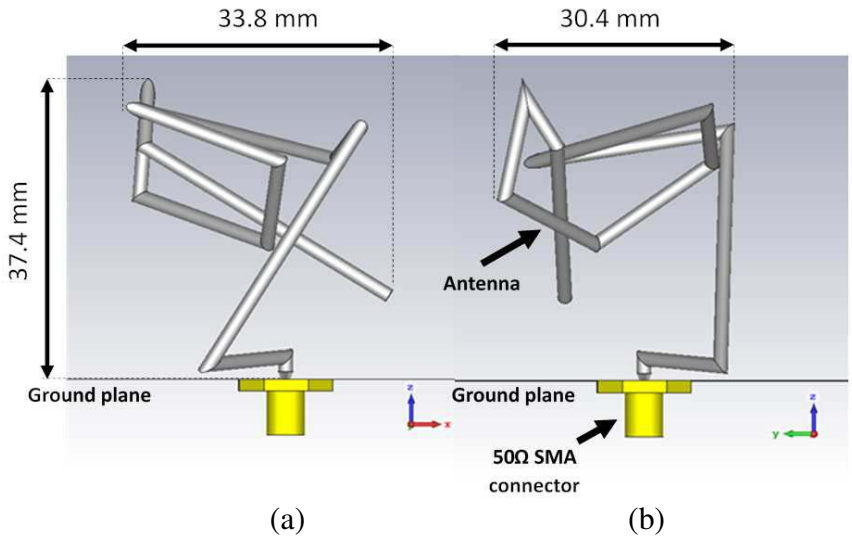

Figure 2. The selected design: (a) *xoz* plane. (b) *yoz* plane.

2.2. Parametric Study

The designed antenna exhibits high geometrical flexibility translated by a high number of parameters. Each of the ten segments constructing the antenna is defined by three parameters (length, azimuth, and elevation angles). This makes the whole structure require 30 parameters to define it. Because it is the last segment, the 10th segment is the most independent part of the antenna geometry since it is connected to only one segment (the 9th). Using this segment's parameter (d_{10}, ϕ_{10}, and θ_{10}), we can tune the antenna response without changing the rest of the structure. Figure 3 shows the impact of d_{10}, ϕ_{10}, and θ_{10} on the simulated reflection coefficient magnitude.

As illustrated in Figure 3(a), we can see that the closer d_{10} is to the optimal value of 39 mm, the better the antenna response is. This was expected since changing the length of the last segment will change the total electrical length of the antenna, which is strongly correlated to its frequency response.

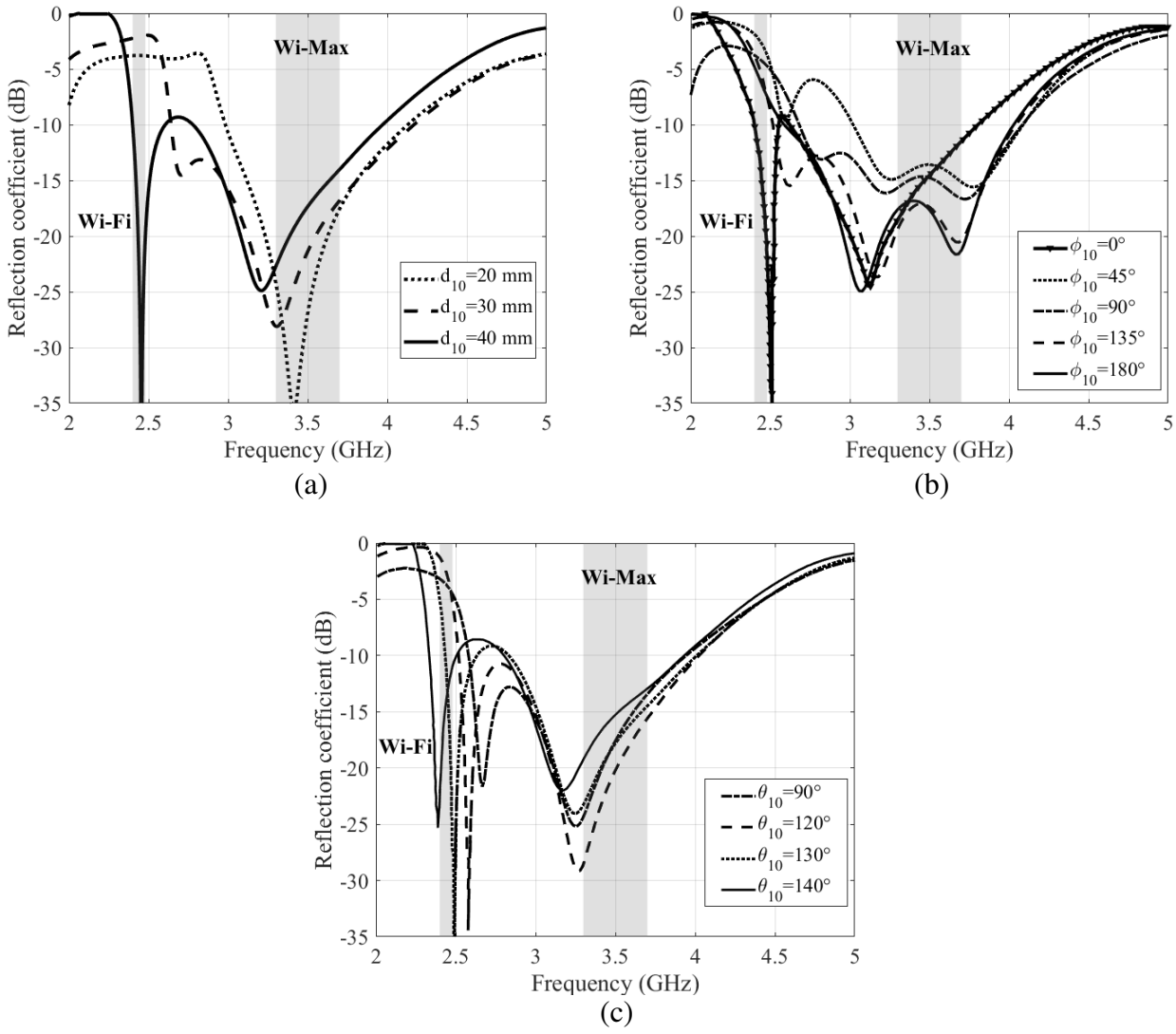

Figure 3. Impact of the 10th segment's parameters (length: d_{10}, azimuth angle: ϕ_{10}, and elevation angle: θ_{10}) on the antenna response. (a) Length. (b) Azimuth angle. (c) Elevation angle.

As shown in Figures 3(b) and 3(c), the variation of ϕ_{10} and θ_{10} is less correlated with the antenna response, notably for the case of θ_{10}. This makes θ_{10} the best parameter to tune to obtain the desired antenna response especially when it comes to the lower band (Wi-Fi) that seems more sensitive to the variations of elevation variant.

We have also studied the impact of the segments' radii (r) on the antenna response, as illustrated in Figure 4. We can see that the radius of the segments (which is considered the same for all segments) has a direct impact on the antenna response. By tuning the segments' radius, we can enhance the impedance matching of the antenna in the desired bands which is translated by a better reflection coefficient. The variation of the radius can also shift the antenna frequency response; however, this remains very limited since the antenna's electrical length is almost unchanged.

2.3. Fabrication of a Prototype

A prototype was fabricated to confirm the simulation results. For this task, a combination of both foundry and 3-D printing techniques was used. The antenna structure was first realized in wax using 3-D printing. The obtained wax structure is buried in sand mixed with binder and water. Outlets are

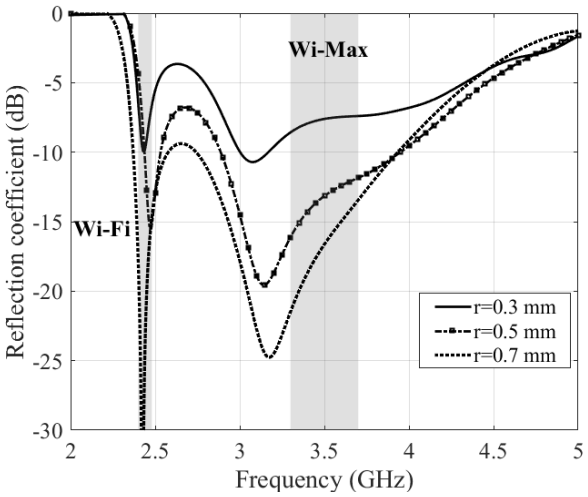

Figure 4. Impact of segments' radius r on the antenna response.

also placed all along the pattern to ensure the exit of the wax when it will be heated up in the presence of molten metal. In the present case, the molten metal is a 90% copper alloy, it is poured through the pouring hole, and it replaces the wax. The metallic structure is cleaned from the casting-sand, and the undesired metallic appendages are removed. A phase of smoothing and surface conditioning is finally done. The resulting shape is very close to the numeric design. It presents some tiny deformations which occurred during the fabrication phase; however, the latter remains negligible compared to the antenna size. The measured radius of the structure is 0.9 mm. The antenna occupies a volume of 33.8 mm $\times$ 30.4 mm $\times$ 37.4 mm ($0.28\lambda_0 \times 0.25\lambda_0 \times 0.30\lambda_0$ where λ_0 is the wavelength at $f = 2.45$ GHz). The total weight of the prototype is only 9 grams, including the SMA connector (6 grams without it). The manufacturing cost of the realized prototype is 25 US dollars (including the SMA connector). Figure 5 shows pictures of the fabricated prototype.

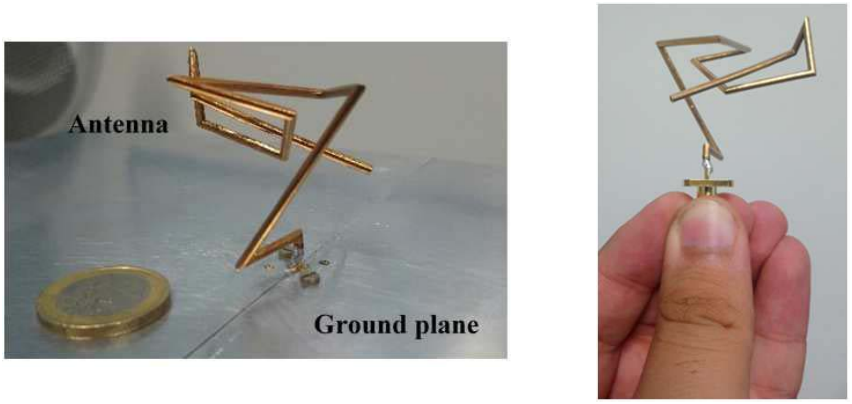

Figure 5. Picture of the fabricated prototypes. (a) Antenna on a ground plane. (b) Antenna alone.

2.4. The Integration of the 3-D Wire Antenna

The 3-D wire antenna is optimized in the existence of a ground plane, which is bulky compared to the size of the antenna. The size of the ground plane is crucial since it guarantees proper matching. Practically, the antenna will be deployed in a metallic entourage that fulfills the task of the ground plane. This removes the need for a large ground plane without degrading the antenna impedance matching. If

we consider a scenario that involves an Unmanned Aerial Vehicle (UAV) of a predominantly metallic structure, the configuration illustrated in Figure 6 is a possible solution. It consists of the creation of a cavity on the UAV's structure to host the antenna. The cavity base should be predominantly metallic and, preferably, connected to the UAV's other metallic parts. The connected metallic parts play the role of a medium-size ground plane that allows to achieve a proper matching. If it is not sufficient, it is possible to enhance the matching using lumped elements or a small matching circuit. Because the antenna is inside a cavity, the UAV's overall dimensions and shape remain unchanged. The cavity could be filled with foam to maintain its aerodynamics.

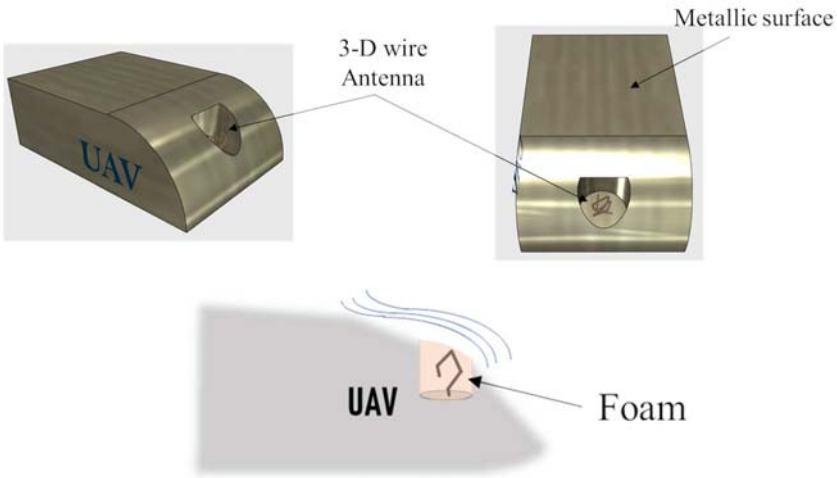

Figure 6. Example of the integration of the 3-D wire antenna above a predominantly metallic device.

3. EXPERIMENTAL VALIDATION

The measured reflection coefficient, S_{11}, of the prototype is compared with the simulated one in Figure 7. The two curves show very similar behaviors. The fabricated prototype presents measured impedance bandwidths at -10 dB that covers 2.36 to 2.55 GHz and 2.78 to 4.43 GHz. The coverage of these bandwidths slightly exceeds the Wi-Fi (2.4–2.483 GHz) bandwidth and largely covers the Wi-Max (3.3–3.7 GHz) one; it is thus very well suited for those communication protocols.

The quality of the CP over the Wi-Max band was experimentally checked. For that, the Axial Ratio (AR) was measured. When it propagates, the electric field of polarized electromagnetic radiation describes, in the most general form, an ellipse. The axial ratio is the ratio of the longer axis of that ellipse to the shorter one. Two special cases exist: linear polarization for which the shorter axis becomes 0 and the CP for which the shorter axis is equal to the longer one. In the last case (and only for that case), the axial ratio is equal to 1 (i.e., 0 dB).

AR at the zenith was measured according to the technique described in [43]. Measurement and simulated values are compared in Figure 8. There is a good agreement between them. Measurements show that the antenna presents a measured -3 dB ARBW of 18.45% (3.19 to 3.84 GHz). It reaches the value of 1.15 dB at 3.50 GHz. The polarization over the lower frequency band (the Wi-Fi one) is elliptic, and the axial ratio is between 7.36 and 7.50 dB.

Gains were also measured and, once again, compared to the simulated ones. As illustrated in Figure 9, the antenna gain varies with the frequency. The measured gain at the lower band is between 5.37 dBi and 5.7 dBi. The values rise in the upper band, from 6.4 to 7.3 dBi. This is expected since the miniaturization factor is higher for the Wi-Fi bandwidth. Above 4.5 GHz, the values of the realized gain are still high (above 4 dBi) although losses related to the impedance mismatching increase. The decrease of the miniaturization factor with the increase of frequency compensates the effect of impedance mismatch. Measured and estimated gain values are in a fair agreement given the precision of the measurement setup used, which is 2 dB.

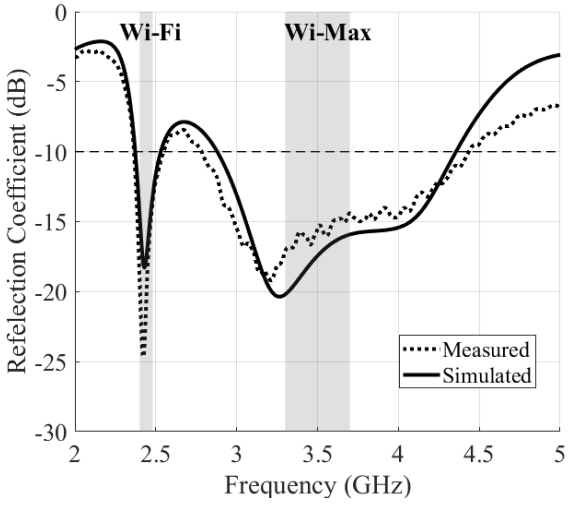

Figure 7. Comparison between simulated and measured coefficient, S_{11}.

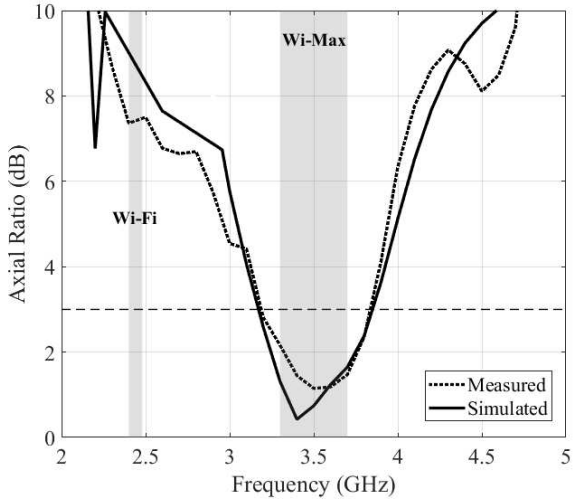

Figure 8. Comparison between simulated and measured axial ratio at the zenith.

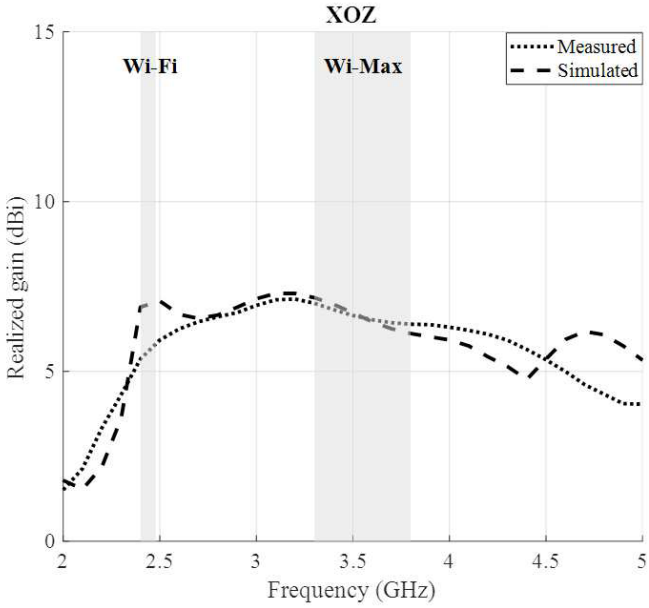

Figure 9. Far-field measurements: simulated and measured maximum gain (xoz plane).

As shown in Figure 10, the radiation patterns were also measured at the targeted bands' central frequencies, 2.45 GHz and 3.5 GHz. At 2.45 GHz, it is the gain of the total power, which is recorded, while at 3.5 GHz, the gain is plotted for the RHCP and LHCP. Those two circular components are calculated from the measurement values according to [43]. The results are shown in Figure 10 and are compared to the simulated radiation patterns. As indicated in Figure 10(b), vertical cuts of the radiations patterns along the planes (xoz) and (yoz) are plotted. Compared to that around 3.5 GHz, the radiation pattern takes a more omnidirectional shape near the frequency of 2.45 GHz. This was expected, in view of the antenna's larger electrical size around the lower frequency. The presence of the ground plane directs the radiation pattern toward the upper hemisphere, which enhances the gain. The maximal gain value at the frequency 2.45 GHz is recorded almost 10° away from the zenith point

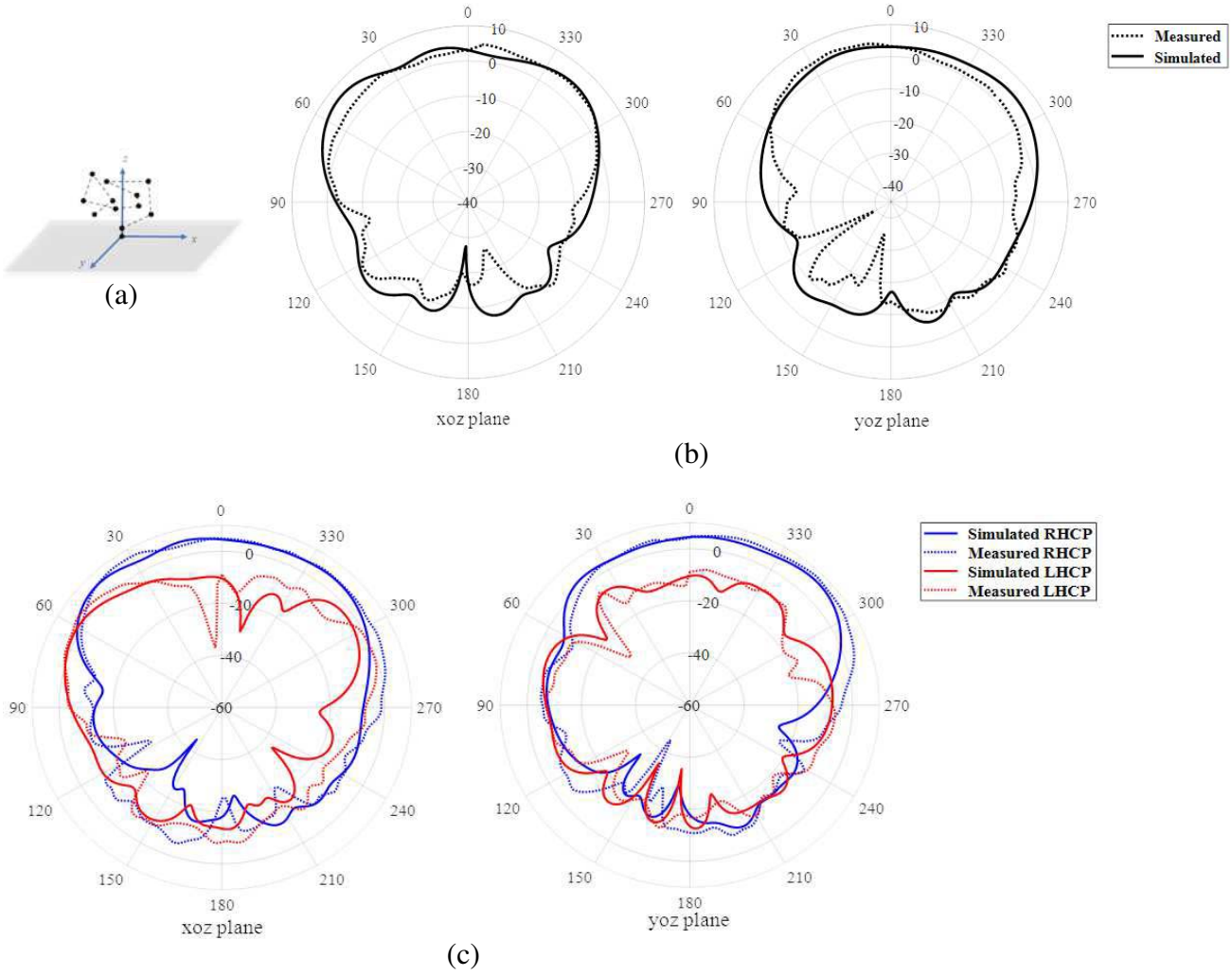

Figure 10. Radiation pattern. (a) Schematic reference. (b) Wi-FI frequency band at $f = 2.45$ GHz. (c) Wi-Max frequency band $f = 3.5$ GHz.

with a measured value of 5.7 dBi (xoz plane). For the Wi-Max band, it was more appealing to illustrate the RHCP and LHCP patterns that reflect the polarization of the characterized antenna. Figure 10(c) shows the simulated and measured patterns in the planes (xoz) and (yoz). As illustrated, the realized antenna exhibits a RHCP that dominates the LHCP component at the elevation directions 60° away from the zenith point with a maximal RHCP gain value higher than 7 dBi. Below the ground plane to almost 30° above the horizon, the antenna loses its CP with comparable magnitudes of LH and RH components, as illustrated in Figure 10(c).

The characteristics of the proposed antenna are compared to those of the existing works in Table 2. The proposed antenna is a good compromise among many different conflicting characteristics: occupied volume, bandwidths, CP, and directivity. It is also very light. Achieving CP at the lower band was a complicated task because of the compactness of the design. The antenna also offers a high radiation efficiency ($> 98\%$) and a high gain. The degradation in the simulated radiation efficiency is a result of the conductivity related losses since we set the antenna material as an annealed lossy copper in the final simulation for more accuracy.

Table 2. Performance comparison with other dual-band antennas.

Ref.	Type	Overall size (λ_0)	-10 dB BW (%)	3 dB ARBW (%)	Max gain (dB)	f_L/f_H (GHz)	Rad. eff. (%)	Construction
[44]	Crossed dipole	$0.64 \times 0.64 \times 0.16$	21.2/9.8	2.9/1.7	7.7/7.4	2.4/3.50	NR	Dielectric based
[13]	Stacked patch	$0.73 \times 0.73 \times 0.05$	9.4/8.7	1.6/2	6.7/7.3	2.75/3.20	$> 70\%$	Dielectric based
[11]	Stacked patch	$0.45 \times 0.45 \times 0.07$	2.3/7.2	0.6/1.4	4.3/6.4	1.61/2.49	NR	Dielectric based
[12]	Stacked patch	$0.50 \times 0.50 \times 0.06$	3/2.7	1.1/1.2	4.5/5.5	0.84/0.92	65–70%	Dielectric based
[14]	Patch + MS	$0.33 \times 0.33 \times 0.04$	7.5/12.6	2.7/2	3.9/5.3	1.88/2.50	NR	Dielectric based
[17]	SIW	$1.47 \times 1.47 \times 0.02$	0.15	1.35/1.45	5.8/4.0	8.84/9.59	$> 92\%$	Dielectric based
[15]	Slot + MS	$0.62 \times 0.58 \times 0.03$	11.7/8	3.2/4.2	6.5/7.0	2.50/3.50	NR	Dielectric based
[16]	Patch	$0.49 \times 0.49 \times 0.02$	1.8/2.6	0.4/0.6	8.4/9.9	2.10/3.60	$> 80\%$	Dielectric based
[18]	ME dipole	$0.98 \times 0.98 \times 0.30$	45/44.6	29.1/13.1	8.5/8.5	2.93/5.35	90–95%	Fully metallic
C.W	3D wire	$0.28 \times 0.25 \times 0.30$	7.53/53.9	-/19.06	5.7/7.3	2.45/3.50	$> 98\%$	Fully metallic

Note: λ_0 is free space wavelength at the operating center frequency of the lower band.

Abbreviations: C.W, Current Work;MS, metasurface; ME, magnetoelectric; SIW, Substrate integrated waveguide. NR, Not Reported.

4. CONCLUSION

A 3-D segmented wire monopole antenna was proposed for Wi-Fi and Wi-Max communication protocols. It has a three-dimensional geometry consisting of ten straight segments distributed randomly in space. It offers features of dual-bands, circular polarization over all the Wi-Max bandwidth, and compactness. Experiment results agree quite well with simulations. The antenna presents high radiation efficiency due to the absence of dielectric materials. Future researches will focus on obtaining the CP over both bandwidths by employing a multi-arm antenna structure.

REFERENCES

1. Feng, B., et al., "HetNet: A flexible architecture for heterogeneous satellite-terrestrial networks," *IEEE Netw.*, Vol. 31, No. 6, 86–92, 2017.
2. Sarma, A., S. Chakraborty, and S. Nandi, "Deciding handover points based on context-aware load balancing in a WiFi-WiMAX heterogeneous network environment," *IEEE Trans. Veh. Technol.*, Vol. 65, No. 1, 348–357, 2016.
3. Meier, R. C., K. Dettloff, and J. G. Waclawsky, "System and method for integrated WiFi/WiMax neighbor AP discovery and AP advertisement," Google Patents, Feb. 12, 2013.
4. Wang, W., X. Liu, J. Vicente, and P. Mohapatra, "Integration gain of heterogeneous WiFi/WiMAX networks," *IEEE Trans. Mob. Comput.*, Vol. 10, No. 8, 1131–1143, 2011.

5. Lin, H., Y. Lin, W. Chang, and R. Cheng, "An integrated WiMAX/WiFi architecture with QoS consistency over broadband wireless networks," *6th IEEE Consumer Communications and Networking Conference*, 1–7, 2009.
6. Niyato, D. and E. Hossain, "Wireless broadband access: WIMAX and beyond — Integration of WiMAX and WiFi: Optimal pricing for bandwidth sharing," *IEEE Commun. Mag.*, Vol. 45, No. 5, 140–146, 2007.
7. Haghighi, M., Z. Qin, D. Carboni, U. Adeel, F. Shi, and J. A. McCann, "Game theoretic and auction-based algorithms towards opportunistic communications in LPWA LoRa networks," *IEEE 3rd World Forum on Internet of Things (WF-IoT)*, 735–740, 2016.
8. Pasolini, G., et al., "Smart city pilot projects using LoRa and IEEE802.15.4 technologies," *Sensors*, Vol. 18, No. 4, 1118, 2018.
9. Lian, L. and L. Li, "Wireless dimming system for LED street lamp based on ZigBee and GPRS," *3rd International Conference on System Science, Engineering Design and Manufacturing Informatization*, Vol. 2, 100–102, 2012.
10. Counselman, C. C., "Multipath-rejecting GPS antennas," *Proc. IEEE*, Vol. 87, No. 1, 86–91, 1999.
11. Chen, K., J. Yuan, and X. Luo, "Compact dual-band dual circularly polarised annular-ring patch antenna for BeiDou navigation satellite system application," *IET Microwaves, Antennas Propag.*, Vol. 11, No. 8, 1079–1085, 2017.
12. Wang, Z., R. She, J. Han, S. Fang, and Y. Liu, "Dual-band dual-sense circularly polarized stacked patch antenna with a small frequency ratio for UHF RFID reader applications," *IEEE Access*, Vol. 5, 15260–15270, 2017.
13. Wang, S., L. Zhu, and W. Wu, "3-D printed inhomogeneous substrate and superstrate for application in dual-band and dual-CP stacked patch antenna," *IEEE Trans. Antennas Propag.*, Vol. 66, No. 5, 2236–2244, 2018.
14. Yue, T., Z. H. Jiang, and D. H. Werner, "A compact metasurface-enabled dual-band dual-circularly polarized antenna loaded with complementary split ring resonators," *IEEE Trans. Antennas Propag.*, Vol. 67, No. 2, 794–803, 2019.
15. Li, K., L. Li, Y. M. Cai, C. Zhu, and C. H. Liang, "A novel design of low-profile dual-band circularly polarized antenna with meta-surface," *IEEE Antennas Wirel. Propag. Lett.*, Vol. 14, 1650–1653, 2015.
16. Liang, Z., D. Yang, X. Wei, and E. Li, "Dual-band dual circularly polarized microstrip antenna with two eccentric rings and an arc-shaped conducting strip," *IEEE Antennas Wirel. Propag. Lett.*, Vol. 15, 834–837, 2016.
17. Kumar, K. and S. Dwari, "Dual-band dual-sense circularly polarized substrate integrated waveguide antenna," *IEEE Antennas Wirel. Propag. Lett.*, Vol. 17, No. 3, 521–524, 2018.
18. Tao, J. and Q. Feng, "Dual-band magnetoelectric dipole antenna with dual-sense circularly polarized character," *IEEE Trans. Antennas Propag.*, Vol. 65, No. 11, 5677–5685, 2017.
19. Le, T. T. and H. H. Tran, "Dual-band dual-sense circularly polarized antenna based on crossed dipole structure for WLAN/WiMAX applications," *Int. J. RF Microw. Comput. Eng.*, Vol. 29, No. 10, e21866, 2019.
20. Altshuler, E. E. and D. S. Linden, "Wire-antenna designs using genetic algorithms," *IEEE Antennas Propag. Mag.*, Vol. 39, No. 2, 33–43, 1997.
21. Best, S. R., "A discussion on the significance of geometry in determining the resonant behavior of fractal and other non-Euclidean wire antennas," *IEEE Antennas Propag. Mag.*, Vol. 45, No. 3, 9–28, 2003.
22. Best, S. R., "A discussion on the quality factor of impedance matched electrically small wire antennas," *IEEE Trans. Antennas Propag.*, Vol. 53, No. 1, 502–508, 2005.
23. Caswell, D. J. and G. B. Lamont, "Wire-antenna geometry design with multiobjective genetic algorithms," *Proceedings of the 2002 Congress on Evolutionary Computation, CEC 2002*, 2002.
24. Altshuler, E. E. and T. H. O'Donnell, "An electrically small multi-frequency genetic antenna immersed in a dielectric powder," *IEEE Antennas Propag. Mag.*, Vol. 53, No. 5, 33–40, 2011.

25. Altshuler, E. E., "Electrically small self-resonant wire antennas optimized using a genetic algorithm," *IEEE Antennas Propag. Mag.*, Vol. 50, No. 3, 297–300, 2002.
26. Altshuler, E. E. and D. S. Linden, "An electrically small genetic antenna immersed in a dielectric," *IEEE Antennas and Propagation Society, AP-S International Symposium (Digest)*, 2007.
27. Benmahmoud, F., P. Lemaitre-Auger, and S. Tedjini, "Design of electrically small 3-D wire antennas for UHF RFID applications using genetic algorithm," *XXXIInd General Assembly and Scientific Symposium of the International Union of Radio Science (URSI GASS)*, 1–4, 2017.
28. Choo, H., R. L. Rogers, and H. Ling, "Design of electrically small wire antennas using a pareto genetic algorithm," *IEEE Trans. Antennas Propag.*, Vol. 53, No. 3, 1038–1046, 2005.
29. Altshuler, E. E. and D. S. Linden, "An ultrawide-band impedance-loaded genetic antenna," *IEEE Trans. Antennas Propag.*, Vol. 52, No. 11, 3147–3151, 2004.
30. Rengarajan, S. R. and Y. Rahmat-Samii, "On the cross-polarization characteristics of crooked wire antennas designed by genetic-algorithms," *IEEE Antennas and Propagation Society, AP-S International Symposium (Digest)*, 2002.
31. Lohn, J. D., D. S. Linden, G. S. Hornby, and W. F. Kraus, "Evolutionary design of an X-band antenna for NASA's space technology 5 mission," *IEEE Antennas and Propagation Society Symposium*, Vol. 3, No. 11, 2313–2316, 2004.
32. Lohn, J. D., G. S. Hornby, and D. S. Linden, "Rapid re-evolution of an X-band antenna for Nasa's space technology 5 mission," *Genetic Programming Theory and Practice III*, 65–78, Springer, US, 2006.
33. Hornby, G., A. Globus, D. Linden, and J. Lohn, "Automated antenna design with evolutionary algorithms," *Space*, Vol. 5, 1–8, 2006.
34. Lohn, J. D., G. S. Hornby, and D. S. Linden, "Human-competitive evolved antennas," *Artif. Intell. Eng. Des. Anal. Manuf. AIEDAM*, Vol. 22, No. 3, 235–247, 2008.
35. Hornby, G. S., J. D. Lohn, and D. S. Linden, "Computer-automated evolution of an X-band antenna for NASA's space technology 5 mission," *Artif. Intell. Eng. Des. Anal. Manuf. AIEDAM*, Vol. 19, No. 1, 1–23, 2010.
36. Lohn, J. D., D. S. Linden, B. Blevins, T. Greenling, and M. R. Allard, "Automated synthesis of a lunar satellite antenna system," *IEEE Trans. Antennas Propag.*, Vol. 63, No. 4, 1436–1444, 2015.
37. G. B. L. and D. A. V. V. Carlos A. Coello, *Evolutionary Algorithms for Solving Multi-objective Problems*, Springer, New York, 2007.
38. Linden, D. S., "Using a real chromosome in a genetic algorithm for wire antenna optimization," *IEEE Antennas and Propagation Society, AP-S International Symposium (Digest)*, 1997.
39. Jin, N. and Y. Rahmat-Samii, "Advances in particle swarm optimization for antenna designs: Real-number, binary, single-objective and multiobjective implementations," *IEEE Trans. Antennas Propag.*, Vol. 55, No. 3, 556–567, 2007.
40. Deb, K., A. Pratap, S. Agarwal, and T. Meyarivan, "A fast and elitist multiobjective genetic algorithm: NSGA-II," *IEEE Trans. Evol. Comput.*, Vol. 6, No. 2, 182–197, 2002.
41. Baumgartner, U., C. Magele, K. Preis, and W. Renhart, "Particle swarm optimisation for Pareto optimal solutions in electromagnetic shape design," *IEE Proc. Sci. Meas. Technol.*, Vol. 40, No. 2, 1172–1175, 2004.
42. Wu, J.-W., J.-Y. Ke, C. F. Jou, and C.-J. Wang, "Microstrip-fed broadband circularly polarised monopole antenna," *IET Microwaves, Antennas Propag.*, Vol. 4, No. 4, 518–525, 2010.
43. Toh, B. Y., R. Cahill, and V. F. Fusco, "Understanding and measuring circular polarization," *IEEE Trans. Educ.*, Vol. 46, No. 3, 313–318, 2003.
44. Le, T. T. and H. H. Tran, "Dual-band dual-sense circularly polarized antenna based on crossed dipole structure for WLAN/WiMAX applications," *Int. J. RF Microw. Comput. Eng.*, Vol. 29, No. 10, 2019.